Predicting plastic events and quantifying the local yield surface in 3D model glasses

Dihui Ruan [a], Sylvain Patinet [b], Michael L. Falk [a,c,d,*]

[a] Department of Materials Science and Engineering, Johns Hopkins University, 3400 North Charles Street, Baltimore, 21218, MD, USA
[b] PMMH, CNRS, ESPCI Paris, Université PSL, Sorbonne Université, Université de Paris, 7 quai St Bernard, Paris, 75005, France
[c] Department of Mechanical Engineering, and Department of Physics and Astronomy, Johns Hopkins University, 3400 North Charles Street, Baltimore, 21218, MD, USA
[d] Hopkins Extreme Materials Institute, Johns Hopkins University, 3400 North Charles Street, Baltimore, 21218, MD, USA

ARTICLE INFO

ABSTRACT

By applying the local yield stress (LYS) method to probe local regions of three-dimensional computational glass models, we confirm high correlations between the measured local yield stress ($\Delta\tau_c$) and the plastic events when the parameterization of the method is properly optimized. The optimal probing region for this system is found to be $\sim 5\sigma$ in radius, where σ represents the Lennard-Jones length scale, approximately the atomic size. The averaged correlation remains positive through the first 200 identified plastic events or 1/3 of the yielding strain ($\sim 7\%$). Here we apply only the local probing that aligns perfectly with the loading on the boundary. The LYS measurements converge to a Weibull distribution with a minimum $\Delta\tau_c$ indistinguishable from zero at larger probing region radii. Analysis of the data in light of an assumption that $\Delta\tau_c$ is a local quantity that obeys extreme value statistics above a critical length scale bounds the exponent of the underlying partial distribution of $\Delta\tau_c \lesssim 0.71$. A thorough investigation of the anisotropy of the local yield surface at the location of the first plastic event indicates that the first triggered region does not align perfectly with the loading on the boundary, but is well-predicted by projecting the shear applied at the boundary onto the local yield surface. This implies that the correlation between the local yield stress prediction and the resulting plasticity may be enhanced by performing a more complete assessment of the local yield surface at each sample point.

1. Introduction

The detailed micro-mechanism of the mechanical response under an elastoplastic deformation in amorphous materials remains poorly characterized relative to their crystalline counterparts in which dislocations can be well specified (Stukowski and Albe, 2010; Shockley and Read, 1949; LeSar, 2014; Püschl, 2002). Falk and Langer (1998) postulated a shear transformation zone (STZ) model in which preexisting defects corresponding to local clusters of atoms/molecules rearrange cooperatively and irreversibly during plastic flow. This STZ concept has been incorporated into constitutive equations for describing elastoplastic behaviors (Bouchbinder et al., 2007b,a; Manning et al., 2007; Bouchbinder and Langer, 2009a,b,c; Rycroft et al., 2015; Hinkle et al., 2017; Kontolati et al., 2021) as well as into discrete models of amorphous plastic response (Homer and Schuh, 2009; Talamali et al., 2012). The existence of such defects in amorphous solids has been supported by experimental studies (Jiang et al., 2011; Ma et al., 2015a,b; Pan et al., 2009) and atomic simulations (Priezjev, 2017; Shi et al., 2007; Shi and Falk, 2005, 2006) in various types of glasses.

Researchers have been keenly interested in how one might accurately locate and characterize such 'flow-defects', and in doing so have measured the correlation of plastic events with a variety of proposed structurally derived predictors.(Richard et al., 2020) These predictors range from trivial structural parameters such as local density (Spaepen, 1977), atomic potential energy (Shi et al., 2007; Hinkle et al., 2017), and short-range order (Shi and Falk, 2005, 2007; Ding et al., 2014a), through more complex metrics obtained via machine learning (Cubuk et al., 2015; Schoenholz et al., 2016), quantification of local excitations induced by linear (Widmer-Cooper et al., 2008; Tanguy et al., 2010; Manning and Liu, 2011; Ding et al., 2014b) or nonlinear (Gartner and Lerner, 2016; Xu et al., 2021) vibrational modes, by probing activation via the minimal energy path (Xu et al., 2017, 2018), and by measurement of local elastic moduli (Tsamados et al., 2009; Mizuno et al., 2013; Shang et al., 2019). Such simulations require a sample sufficiently large to resolve multiple individual STZs. Most of these investigations considered two-dimensional glasses consisting of $\sim 10,000$ atoms. Few analyses in three-dimensional glasses have been performed at comparable length scales, as this requires million-atom simulations prepared by quenching a liquid sufficiently slowly to produce a glass stable enough to compare with experiments.(Shi and Falk, 2007; Ding et al., 2014a,b; Cubuk et al., 2015; Schoenholz et al., 2016)

In the context of the above indicators, Patinet et al. (2016) and Barbot et al. (2018) developed the local yield stress (LYS) method in which local regions are sheared at a particular length scale and loading orientation until yielding is triggered. By measuring the incremental stress to yield, the LYS method provides a direct measurement of elastoplastic response. High correlations have been observed between low local yield stresses and the sites where plastic events are observed during subsequent shear simulations of the material as a whole. A recent comparison found that this method ranks highly among a large number of structural indicators in 2D glassy samples, and performs best amongst these comparators in deeply quenched glasses, those modeled samples most comparable to as-quenched glasses produced in laboratory and industrial processes.(Richard et al., 2020) The LYS framework also quantifies atomistic data in ways that clearly relate to the yield surface, a continuum concept critical for understanding plasticity at the macro-scale (Lund and Schuh, 2003; Schuh and Lund, 2003). Characterizing larger 3D glasses has presented a challenge for diagonalization-based methods such as the identification of 'soft' spots in Manning and Liu (2011). Recent advances have provided more efficient ways to explore low-frequency modes to locate STZs, but comprehensive characterization of a material using such methods remains a challenge (Richard et al., 2021). The computational expense for the LYS method scales with the system size as $\mathcal{O}(N)$ making it applicable to these larger three-dimensional systems.

Here we apply the LYS method to measure spatial variations in the incremental stress to yield ($\Delta\tau_c$) along a single local probing determined by a strain tensor. The resulting measurements of $\Delta\tau_c$ exhibit a correlation with the locations of the local plastic events produced by a similarly oriented strain applied at the boundary. The correlation persists until about $1/3$ of the yielding strain when undertaken at the optimal length scale, $\sim 5\sigma$(atomic diameters) in radius.

Variation in the local probing strain is also examined at the location of the first identified plastic event. These data indicate that the triaxiality, orientation, rotation, and sign of the resulting plastic event aligns well with what one would infer from the measured local yield surface, but does not exactly correspond with the strain applied at the boundary. This suggests that the correlation of $\Delta\tau_c$ with the observed plastic events would improve if the entire local yield stress surface, rather than only the value of $\Delta\tau_c$ along the direction of the applied shear, were to be characterized throughout the material.

2. Sample preparation

We perform molecular dynamics (MD) simulations to prepare three independent Kob–Andersen(KA) (Kob and Andersen, 1995) binary Lennard-Jones (LJ) glasses within the Large-scale Atomic/Molecular Massively Parallel Simulator (LAMMPS) environment (LAMMPS). In each sample, 1,000,000 atoms are simulated in a cubic simulation box with periodic boundary conditions along the x, y and z axes. The system is comprised of 80% large atoms (A) and 20% small atoms (B). We apply a smoothed 6–12 Lennard-Jones(LJ) potential (Jones and Chapman, 1924) field to quantify the interatomic interactions.

According to a prior study by Shi and Falk (2006), shear bands only arise during deformation in KA glasses prepared with relatively low quenching rates. To focus on KA glasses susceptible to strain localization, we follow the same preparation procedure to melt and equilibrate the initial configuration at a reservoir temperature $T = 0.87\epsilon/k_B$ under an external pressure $P = 8.5\epsilon/\sigma^3$, and we then cool this melt to $T = 0.03\epsilon/k_B$ while releasing the pressure to $P = 0\epsilon/\sigma^3$ linearly over a duration of $2000t_0$ using a Nose–Hoover thermostat (Nosé, 1984; Hoover, 1985) and Parrinello-Rahman barostat (Parrinello and Rahman, 1981). We verify that the difference in the potential energy per atom at the as-quenched state between our samples and the corresponding KA glasses in Shi and Falk (2006) results from our choice of the smoothed LJ potential and the difference in the aspect ratio of the box dimension. Minimization of the energy via a conjugate gradient scheme (Polak and Ribiere, 1969) under zero pressure conditions is undertaken until achieving the convergence of the total force norm of the whole system. This is followed by a second force minimization with constrained volume for studying the athermal mechanical response at zero temperature. The final box dimension of these three KA glasses is approximately $93.4\sigma \times 93.4\sigma \times 93.4\sigma$, where x and y dimensions are comparable to those of the 2D systems previously studied by the local yield stress method (Barbot et al., 2018; Patinet et al., 2016). The configurations of all 3 glasses can be found on Johns Hopkins University Data Archive (Ruan et al., 2021).

3. Three-dimensional local yield stresses

3.1. 3D Local yield stress method

Patinet et al. developed the local yield stress (LYS) method in Patinet et al. (2016) based upon the assumption that plastic events in amorphous solids occur as localized rearrangements located at STZs (Falk and Langer, 1998). In the LYS method, local regions of
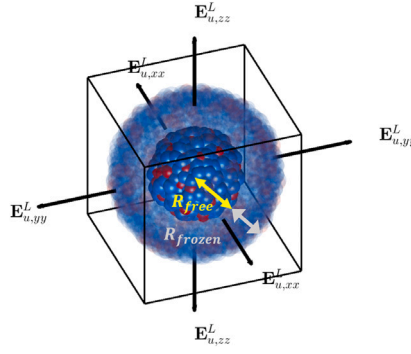
Fig. 1. Schematics of a spherical region of atoms cut from the simulation box for local probing in a 3D binary glass with large (blue) and small (red) particles. The atoms in transparency form a shell of the core atoms shown in solid color. R_{free} and R_{frozen} are labeled by arrows in yellow and gray respectively. The black arrows denote the loading on the local boundary in Eq. (6).

atoms are sheared to the point of mechanical instability identified by a stress drop, and the incremental stress required to reach the yielding point is recorded as the local yield stress ($\Delta\tau_c$). A low value of $\Delta\tau_c$ indicates relative high susceptibility to plasticity. In our three-dimensional LYS analyses, spherical regions of atoms within a radius $R_{free} + R_{frozen}$ are probed by the athermal quasi-static (AQS) method (Tanguy et al., 2006; Lerner and Procaccia, 2009; Tsamados et al., 2009; Dasgupta et al., 2012; Karmakar et al., 2010; Maloney and Lemaître, 2004). The atoms in the inner core with radius R_{free} are referred to as the 'free' atoms, and the atoms in the outer shell with thickness R_{frozen} are referred to as the 'frozen' atoms, as is shown in Fig. 1. At each increment of loading, the 'frozen' atoms are deformed affinely with respect to the probing strain, and the 'free' atoms bounded by the 'frozen' shell undergo static relaxation into the nearest mechanically stable configuration using a conjugate gradient method (Polak and Ribiere, 1969). R_{frozen} is set to be 5σ, twice the smoothed LJ potential cutoff radius $r_{out} = 2.5\sigma$, to include all relevant neighbor atoms for the 'free' atoms.

An increment of local loading ΔE^L with a constant volume can be written in terms of a strain step magnitude Δe^L multiplied by a unit local strain tensor E_u^L as

$$\Delta E^L = \Delta e^L E_u^L. \tag{1}$$

All strains are expressed as Lagrange strains defined relative to the initial undeformed configuration. The projected stress τ_p is defined as

$$\tau_p = S^L : E_u^L, \tag{2}$$

where S^L is the Cauchy stress tensor of the local 'free' region. Since the system is loaded along the principal axes and the volume is held constant, this is equivalent to the Kirchhoff stress. The most appropriate way to quantify continuum fluxes like stress from atomistic data remains an area of active research (Chen and Diaz, 2018). Here we resort to the widely used virial approximation to quantify stress within the region of interest. In the athermal limit (Heyes, 1994; Sirk et al., 2013; Thompson et al., 2009; Surblys et al., 2019), the virial contribution of atom i can be computed as a tensor

$$\Phi_i = \frac{1}{2} \sum_{j \neq i}^{N_p} \left(\vec{r}_{ij} \otimes \vec{f}_{ij} \right), \tag{3}$$

in which atom j is one of N_p atoms within the pairwise potential cutoff radius from atom i. The displacement vector $\vec{r}_{ij} = \vec{r}_j - \vec{r}_i$ represents the interatomic displacement, and $\vec{f}_{ij}$ represents the force exerted on atom i from atom j. S^L can then be estimated by dividing the sum of the virial contributions Φ_i from the N_{free} atoms in the free region by its volume as

$$S^L \approx \frac{3}{4\pi R_{free}^3} \sum_{i=1}^{N_{free}} \Phi_i. \tag{4}$$

The projected stress τ_p is used to identify whether the response to an incremental strain is elastic or if, rather, an instability has been triggered. The stress tensor at the point when a stress drop is detected will be referred to as the onset stress S_{onset}^L. This stress is used to calculate the local yield stress $\Delta\tau_c$ given by

$$\Delta\tau_c = (S_{onset}^L - S_0^L) : E_u^L, \tag{5}$$

where S_0^L is the initial stress state of the local region before any probing. It is important to note that due to the residual stresses present in glasses, the elements in the initial undeformed stress tensor S_0^L are typically not equal to zero. Since undertaking the local yield stress analysis in 3D is computationally demanding, we initially limit our investigation to the case where E_u^L is chosen

Table 1

Table of initial force tolerance F_{tol}^0, strain step Δe^L, and final force tolerance F_{tol} settings at each R_{free}. *: Δe^L (10^{-6}) is the smallest strain step achievable computationally given the available resources.

$R_{free}(\sigma)$	$F_{tol}^0(\epsilon/\sigma)$	Δe^L	$F_{tol}(\epsilon/\sigma)$
2.5	2×10^{-11}	10^{-4}	10^{-6}
3.75	3×10^{-11}	10^{-4}	10^{-6}
5	4×10^{-11}	10^{-5}	10^{-6}
7.5	8×10^{-11}	10^{-6} *	10^{-6}
10	2×10^{-10}	10^{-6} *	10^{-6}

to be a pure shear loading as

$$E_u^L = \frac{\sqrt{2}}{2}\begin{bmatrix} 1 & 0 & 0 \\ 0 & -1 & 0 \\ 0 & 0 & 0 \end{bmatrix}. \tag{6}$$

To impose strain, equal tension and compression are applied along the x axis and the y axis while zero strain is imposed along the z axis, as illustrated in Fig. 1. This plane strain boundary condition is comparable to the prior study on the 2D local yield stress method in Patinet et al. (2016) and Barbot et al. (2018).

3.2. Parameterization

The LYS method involves probing local regions with respect to a local unit strain tensor E_u^L and measuring the incremental stress required to induce a local instability. There are three parameters playing important roles in computing the local yield stress $\Delta\tau_c$: the force tolerance F_{tol} that sets the accuracy of force minimization when relaxing the 'free' atoms, the strain step Δe^L that controls the magnitude of each increment of loading, and the characteristic length R_{free} that determines the sizes of locally probed regions. The optimal values of these three parameters are not independent of each other. For instance, for larger R_{free} values, more atoms may participate in the plastic rearrangement, and the higher number of degrees of freedom necessitates a smaller strain step Δe^L.(Karmakar et al., 2010)

In Table 1, we list the parameters that are obtained from a series of convergence studies that we have undertaken to optimize the parameters. All the convergence studies are executed on sampling regions centered on evenly spaced $2 \times 2 \times 2$ grids extracted from the binary LJ glass samples described in **Materials and Methods**. For each listed R_{free} between 2.5σ and 10σ, an initial force tolerance F_{tol}^0 is chosen by sampling the convergence of the force norm when probing a very small strain 10^{-7}. Local yield stresses ($\Delta\tau_c$) are computed at various strain steps Δe^L, and these results are compared with the results using the smallest Δe^L (10^{-6}) we could achieve within our computational limitations. We choose the largest strain step Δe^L that results in a relative difference in $\Delta\tau_c$ $\leqslant 1\%$ or we choose 10^{-6}, as noted in Table 1. With Δe^L set, we raise the values of F_{tol} to enhance the computational efficiency in the 3D LYS method. The final F_{tol} settings are determined by converging the computed $\Delta\tau_c$ with various F_{tol} values to be within $\leqslant 1\%$ of the results using F_{tol}^0. We are able to raise the final F_{tol} values to 10^{-6} among all the R_{free} values without significantly affecting the results.

3.3. Distribution and scaling

In order to uniformly sample the material response, local yield stresses ($\Delta\tau_c$) are computed in probing regions centered on evenly spaced grid points throughout the simulation box instead of probing regions centered on each atom as had been done in prior 2D studies (Patinet et al., 2016). The distance between grid points d_{sample} is chosen as $\sim 10\sigma$ to approach a set of $10 \times 10 \times 10$ samples in each Kob–Anderson (KA) (Kob and Andersen, 1995) glass. From these samples, we are able to compute the distribution of $\Delta\tau_c$ in a representative manner. The distributions of local yield stress ($\Delta\tau_c$) with R_{free} from 2.5σ to 10σ are plotted in the inset of Fig. 2(a). As was observed in the prior 2D studies (Patinet et al., 2016; Barbot et al., 2018), increasing R_{free} results in more sampling regions yielding at lower $\Delta\tau_c$, and the peaks of these probability density functions (P_d) shift toward lower $\Delta\tau_c$ values with heavier low-end tails. This is consistent with our expectation that yielding behavior is controlled by the easiest to yield STZ in the sampling region. If we consider yield to be a local phenomenon, such that STZs are independent above a critical length scale (R_{free}^c), larger regions are expected to incorporate more STZs, and their $\Delta\tau_c$ should be lower on average than that of smaller regions that contain fewer STZs. If we assume that the observed yield stress is determined by the STZ with the lowest yield stress in the region, $\Delta\tau_c$ of a larger region is the minimum $\Delta\tau_c$ of all the included regions.

To test this assumption of 'isolated' local yield regions, we compare these distributions to the 'Extreme Value Distribution' (EVD) (Gumbel, 2004), which categorizes the distribution of maxima or minima of random variables. Since $\Delta\tau_c$ is defined to be non-negative, minima of sampled $\Delta\tau_c$ values are expected to result in a Weibull distribution when sampled at a length scale sufficiently larger than the scale on which distinct sub-regions would be independent.(Weibull and Stockholm, 1951) For sufficiently large
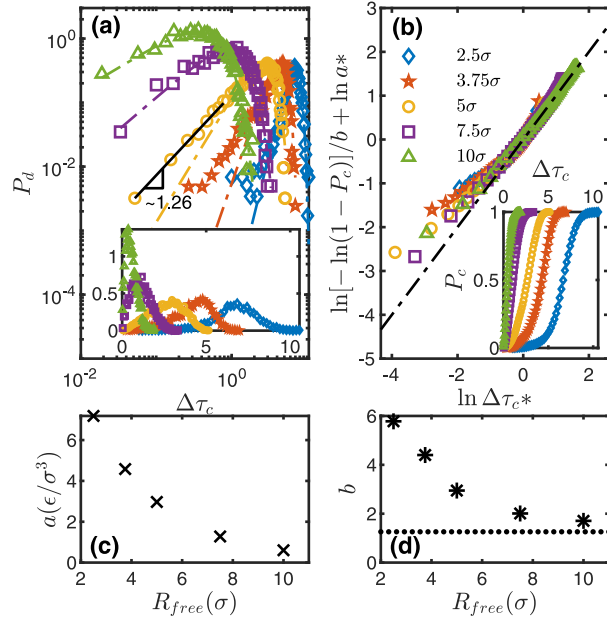
Fig. 2. Local yield stress ($\Delta\tau_c$) distributions with $R_{free} = 2.5\sigma(\diamond)$, $3.75\sigma(\star)$, $5\sigma(\circ)$, $7.5\sigma(\square)$, and $10\sigma(\triangle)$. (a) Log–log plot of $\Delta\tau_c$ probability density function (P_d). Dot-dashed lines denote Weibull distribution fits (Eq. (7)). The black solid line denotes the slope of the log–log distribution at $\Delta\tau_c \to 0$ with $R_{free} = 5\sigma$. Inset: linear–linear plot of the probability density function of $\Delta\tau_c$. (b) Scaled plot of the normalized cumulative distribution function of $\Delta\tau_c$, where the dot-dashed line denotes for a linear guideline extrapolated from $\Delta\tau_c$ distribution with $R_{free} = 10\sigma$. *: The curves are shifted by their corresponding modes. Inset: the cumulative distribution of $\Delta\tau_c$. Plot of (c) the scale parameter a (×) and (d) the shape parameter b (*) from the Weibull distribution fits in Fig. 2 versus R_{free}. The dotted line in (d) denotes the lower bound for b to converge with extremely large R_{free}.

Source: The original data in this figure can be found on Johns Hopkins University Data Archive (Ruan et al., 2021).

sampling regions, the probability density function (P_d) and cumulative distribution function (P_c) are therefore expected to be given by

$$P_d(\Delta\tau_c|a,b) = \frac{b}{a}\left(\frac{\Delta\tau_c}{a}\right)^{b-1}\exp\left[-\left(\frac{\Delta\tau_c}{a}\right)^b\right], \tag{7}$$

and

$$P_c(\Delta\tau_c|a,b) = 1 - \exp\left[-\left(\frac{\Delta\tau_c}{a}\right)^b\right], \tag{8}$$

where a is the scale parameter, and b is the shape parameter. As is presented in Fig. 2(c), the scale parameter a is observed to decrease with increasing R_{free} corresponding to a lower mean when a larger local region is probed. Here, the shape parameter $b > 1$ indicates that the instantaneous 'yield rate'

$$M(\Delta\tau_c|a,b) = \frac{P_d(\Delta\tau_c)}{1 - P_c(\Delta\tau_c)} = \frac{b}{a}\left(\frac{\Delta\tau_c}{a}\right)^{b-1}, \tag{9}$$

the number of yield events per unit stress, increases with $\Delta\tau_c$.(Jiang and Murthy, 2011)

The fitted Weibull distributions are plotted as dot-dashed lines on top of the measured $\Delta\tau_c$ distributions in the main plot of Fig. 2(a). Also, the corresponding cumulative distributions (P_c) of $\Delta\tau_c$ are presented in the inset of Fig. 2(b). In the main plot of Fig. 2(b), the cumulative distributions of $\Delta\tau_c$ are normalized by the two fitting parameters a and b in terms of $\ln\left[-\ln\left(1 - P_c\right)\right]/b + \ln a$ and are then plotted versus $\ln\Delta\tau_c$ after being shifted by the corresponding mode. Combining the above plots, we notice that the distributions of $\Delta\tau_c$ align with the Weibull distribution for larger R_{free} values. More specifically, the density distribution functions in Fig. 2(a) with $R_{free} = 7.5\sigma$ and 10σ are significantly Weibull-like. Therefore, the underlying distribution of $\Delta\tau_c$ at some critical length with R_{free}^c under 7.5σ is inferred to behave like a power-law distribution in the limit of $\Delta\tau_c \to 0$.(Hansen and Roux, 2000)

Close inspection of the data taken with R_{free} from 2.5σ to 3.75σ, reveals that the lower-value tails of their probability density functions deviate from the power law form that would be expected to lead to a Weibull distribution. These distributions discontinuously drop to zero below a relatively high threshold, as shown in the main plot of Fig. 2(a). We believe this indicates that lower $\Delta\tau_c$ values cannot be accurately measured due to the limitations that the boundary constraints impose on local rearrangements within smaller regions. In comparison, the smooth $\Delta\tau_c$ distribution at $R_{free} = 5\sigma$ behaves like a power-law distribution as $\Delta\tau_c \to 0$. Notably, this distribution does not converge to a Weibull distribution. In addition, we note that the power-law of the partial distribution function is 1.26 as shown by the slope of the log–log distribution at the lower end when $R_{free} = 5\sigma$ in Fig. 2(a).
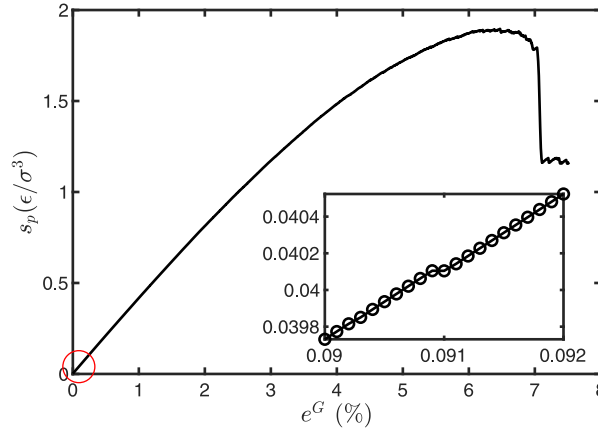
Fig. 3. Stress–strain response for the AQS deformation with a strain step $\Delta e^G = 10^{-6}$ on one KA glass. The inset is the zoom-in view of the circled region in the main plot, where the first plastic event is identified.
Source: The original data of the stress–strain response for all 3 independent glasses can be found on Johns Hopkins University Data Archive (Ruan et al., 2021).

The shape parameter b used to fit the Weibull distribution to the data in Fig. 2(d) should converge to $1 + \eta$ where η is the exponent of the underlying density distribution, i.e. b should approach 2.26.(Hansen and Roux, 2000) In Fig. 2(d) we see that the value of b from the fitted Weibull distribution converges to a value $\lesssim 1.71$. We note that this exponent matches closely a previous numerical estimate based on extreme value analysis (Karmakar et al., 2010) and the prediction made by Kapteijns, Richard and Lerner for nonlinear quasilocalized excitations. (Kapteijns et al., 2020)

Furthermore, based on the derivation of the extreme value statistics, the mean $\Delta \tau_c$ when probing larger regions whose size is far above the critical length R_{free}^c can be related to the cumulative distribution P_c^* in terms of N, the number of STZs in the probing region as Hansen and Roux (2000)

$$\langle \Delta \tau_c \rangle = P_c^{*-1} \left(\frac{1}{N+1} \right). \tag{10}$$

If we suppose R_{free}^c to be 5σ, $N(R_{free} = 7.5\sigma) \approx 11$ and $N(R_{free} = 10\sigma) \approx 47$ accordingly. While we intuitively expect that $N \propto R_{free}^3$, this is not consistent with the above two R_{free} values. This inconsistency combined with the discrepancy between the Weibull fit and the exponent of the tail of the underlying distribution argues against the applicability of a simple "weakest link" picture for quantitatively understanding the statistics of STZs. We further discuss the consequences of this observation in our conclusions.

4. Locating plastic events

To identify the series of plastic events that arise during loading, the simulation box is deformed via the AQS method. At each strain step, the simulation box and the atoms are affinely deformed. All atoms are then relaxed to their mechanically equilibrated state. The conjugate gradient method is deployed to minimize the forces during the relaxation. The load on the boundary is applied in the same manner as the locally-probed deformation described by Eq. (6). At each strain step applied on the boundary (Δe^G), a projected stress for the simulation box (s_p) is recorded to characterize the stress–strain response,

$$s_p = S^G : E_u^G, \tag{11}$$

where E_u^G denotes the unit global strain tensor. The Cauchy stress of the system is approximated by the virial expression, $S^G \approx \frac{1}{V} \sum_{i=1}^{N} \Phi_i$, where V is the volume of the simulation box and N is the total number of atoms in the system. A plastic event is identified by each instance in which the stress (i.e., s_p) decreases. These 3D KA glasses exhibit a discontinuous drop in the stress due to strain localization at approximately 7% strain with strain step 10^{-6}, as is indicated in Fig. 3. Due to the relatively large size of these 3D systems, many plastic events are triggered during deformation. This makes the serrations difficult to resolve by eye, in contrast to the obvious fluctuations in some previously studied 2D glasses (Barbot et al., 2018). The inset presents the first identified plastic event with a stress drop of $\sim 5.30 \times 10^{-7} \epsilon/\sigma^3$ and a triggering strain of $\sim 0.091\%$. As was noted in Salerno and Robbins (2013), the identified plastic events depend on the strain step. This means that smaller and smaller plastic events are observed to occur at smaller and smaller strain as the strain step is decreased. Due to computational limitations, it is not possible to converge Δe^G to determine if there is a 'true' first plastic event in our prepared glasses with 1,000,000 atoms, and answering that question is not the objective of this work. Rather we assume that the strain step determines the resolution at which we are able to sample plastic rearrangements during deformation of the simulation box. We apply the loading on the boundary with the smallest strain step which is computationally affordable (10^{-7}) until the first stress drop in an effort to characterize the smallest length scale at which 3D Hooke's law behavior is recovered. For testing the predictivity of the LYS method, consecutive plastic events are sampled every 10^{-6} strain.
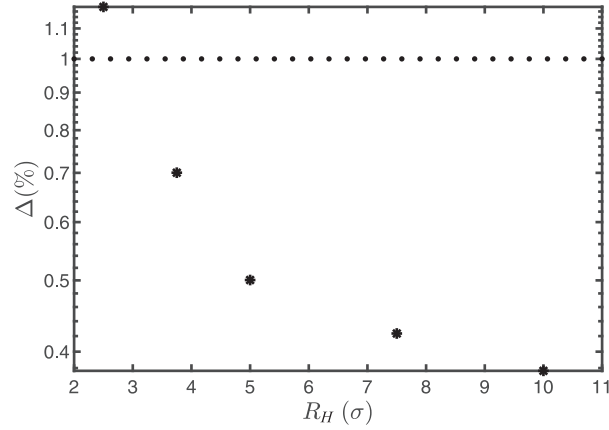
Fig. 4. Log-linear plot of deviation from 3D Hooke's law versus averaging radius R_H. The standard errors are negligible compared with the size of the markers. The dotted line is the guideline for 1%.

5. Deviation from Hooke's law

In determining the region size set by R_{free}, the local yield stress method assumes that Hooke's law is valid at this length scale. An evaluation of the consistency of local material response with Hooke's law should thus set a lower bound on R_{free} in computing the local yield stresses ($\Delta\tau_c$). Here, we adopt the methodology developed by Tsamados et al. (2009) to estimate the deviation from linear elasticity at a given length scale. The whole simulation box is deformed in increments of 10^{-7} strain. The virial contribution at each atom (Eq. (3)) is computed both at the initial as-quenched state ($\Phi_{i,0}^G$) and at the first onset of instability ($\Phi_{i,y}^G$), defined as the configuration prior to the first stress drop (at $0.012 \pm 0.007\%$). Instead of applying a Gaussian windowing function as in Tsamados et al. (2009), we sum these local contributions from N_H atoms within the sampling radius R_H, to remain consistent with the uniform contributions from the 'free' atoms when computing the local yield stress ($\Delta\tau_c$). The Cauchy stress change in this region is then approximated by

$$S_{i,R_H}^G = \frac{3}{4\pi R_H^3} \sum_j^{N_H} \left(\Phi_{j,y}^G - \Phi_{j,0}^G \right). \tag{12}$$

By comparing the above two configurations, the atomic strain tensor centered at each atom is calculated with varying cutoff radii R_H according to Falk and Langer (1998) and Shimizu et al. (2007) using the OVITO open visualization tool (Stukowski, 2010). A deformation gradient tensor F_i is computed by minimizing

$$\sum_{j=1}^{N_H} \left| \vec{r}_{ij,0} F_i - \vec{r}_{ij,y} \right|^2, \tag{13}$$

where $\vec{r}_{ij,0}$ and $\vec{r}_{ij,y}$ are displacement vectors between atom j and i in the unstrained state and at the onset of instability respectively.(Shimizu et al., 2007) It follows that

$$F_i = \left(\sum_{j=1}^{N_H} \vec{r}_{ij,0} \otimes \vec{r}_{ij,0} \right)^{-1} \left(\sum_{j=1}^{N_H} \vec{r}_{ij,0} \otimes \vec{r}_{ij,y} \right). \tag{14}$$

The resulting atomic strain tensor centered at atom i is then calculated as

$$\varepsilon_{i,R_H}^G = \frac{1}{2} \left(F_i^T F_i - I \right). \tag{15}$$

Here we denote the strain as ε to emphasize that since all strains are on the order of 0.01% we are operating in the limit of infinitesimal strains where all stress and strain measures are essentially equivalent. Consider the generalized 3D Hooke's law in Voigt notation

$$\tilde{S} = \tilde{C}\tilde{\varepsilon} \tag{16}$$

where, for instance, s_{xx} in $\tilde{S}$ and ε_{xx} in $\tilde{\varepsilon}$ represent the stress and strain components along x direction on the yz plane, and c_{ijkl} in $\tilde{C}$ denotes one of the 21 nonzero elastic constants from a 4th order elastic-moduli tensor. To solve for these 21 unknowns in the stiffness matrix, 21 linear equations must be generated from 4 independent deformations. The resulting solution is, in general, overdetermined. We apply the least-squares method (Paige and Saunders, 1982) to optimize the 21 elastic moduli numerically. Preset bounds on the solutions are applied with regards to the bulk stiffness matrix of the whole system.
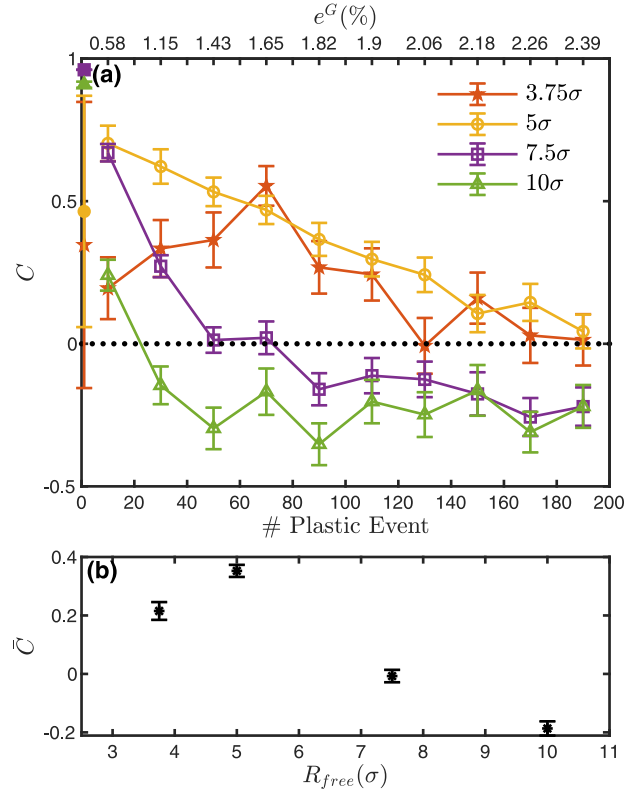
Fig. 5. (a) Plot of correlation from Eq. (20) versus the Nth plastic event with $3.75\sigma(\star)$, $5\sigma(\circ)$, $7.5\sigma(\square)$, and $10\sigma(\triangle)$. The hollow markers denote data points averaged over every 20 plastic events for 3 independent KA glasses. The 4 solid markers denote the mean correlation over the 3 glasses at the 1st plastic event. The standard errors are presented by the errorbars. The upper x-axis marks the corresponding triggering strain for each averaged correlation. The dotted line denotes $C = 0$. (b) Plot of the correlation averaged over all the plastic events in (a) versus R_{free}, with standard errors denoted by errorbars. The correlation with $R_{free} = 2.5\sigma$ is excluded due to its relatively large deviation from Hooke's law (see Fig. 4).

We then perform 11 independent deformations on the simulation box with the unit strain tensor

$$\epsilon_u^G = \frac{\sqrt{2\psi^2 - 4\psi + 8}}{\psi^2 - 2\psi + 4} \begin{bmatrix} 1 & 0 & 0 \\ 0 & \frac{\psi}{2} - 1 & 0 \\ 0 & 0 & -\frac{\psi}{2} \end{bmatrix}, \tag{17}$$

in which triaxiality $\psi = 0, 0.1, 0.2, 0.3, \ldots, 1$. For an atom i, the deformations with ψ ranging from 0.1 to 1 overdetermine the elastic constants in Eq. (16). The length scale dependence of the overdetermined elastic constants is assessed by varying R_H from 2.5 to 10σ. At $\psi = 0$, an estimated stress tensor $\tilde{S}_{i,R_H}^{G'}$ (in Voigt notation) is calculated by substituting the solved stiffness matrix and the strain tensor into Eq. (16). Then $\tilde{S}_{i,R_H}^{G'}$ is compared with the directly computed stress tensor $\tilde{S}_{i,R_H}^{G}$ and its deviation is quantified by the relative root mean square as

$$\Delta_{i,R_H} = \sqrt{\frac{\left\| \tilde{S}_{i,R_H}^{G'} - \tilde{S}_{i,R_H}^{G} \right\|^2}{6 \left\| \tilde{S}_{i,R_H}^{G} \right\|^2}}. \tag{18}$$

In Fig. 4, the mean deviation averaged among all the atoms are plotted against the averaging radius R_H. If we choose the threshold for elastic behavior to be $\leq 1\%$ as in Tsamados et al. (2009), then the 3D Hooke's law is valid at a length scale R_H above 2.5σ, which can thus serve as the lower limit of R_{free} for the local yield stress method in the 3D glasses.

6. Correlation between $\Delta\tau_c$ and plastic events

Next, we would like to assess the degree of correlation of the localized plasticity with the local yield stress, and in doing so determine an optimal length scale for R_{free}. We consider multiple plastic events obtained by shearing with strain steps $\Delta e^G = 10^{-6}$. Each plastic event is identified by a stress (s_p) drop, and the yield point is recorded as the last configuration prior to instability.
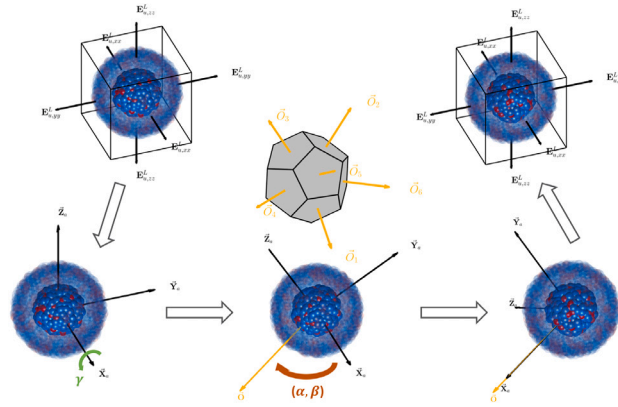
Fig. 6. Schematics of rotating and probing a local region. The 'frozen' atoms in transparency form a shell of the core 'free' atoms shown in solid color. The black arrows on the local boundary denote the loading given by E_u^L in Eq. (22) before (upper left) and after (upper right) the rotation. $(\vec{X}_a, \vec{Y}_a, \vec{Z}_a)$ represents for the coordinate system of the atoms rotating about $\vec{X}_a$ counter-clockwise with angle γ (green arrows) and then aligning $\vec{X}_a$ with a direction $\vec{O}$ (yellow arrows). $\vec{O}$ (yellow arrows) is sampled with respect to the face norms in a regular dodecahedron in the middle.

Considering two consecutive events, the end of the former event also serves as the reference point of the subsequent event, which is identified as the last configuration prior to a stress (s_p) increase after a relaxation. We locate the triggered plastic rearrangement and characterize its nature by comparing the configuration after relaxation to the configuration at the yield point. These two configurations are denoted by subscripts e, for end, and y, for yield, respectively. At each atom, the deviation from affinity D_{min}^2 is calculated as

$$D_{min,i}^2 = \sum_{j=1}^{N_{cut}} \left| \vec{r}_{ij,y} \boldsymbol{F}_i - \vec{r}_{ij,e} \right|^2, \tag{19}$$

where, we solve for $\boldsymbol{F}_i$ as described in Eq. (14). N_{cut} is the number of neighbor atoms within a cutoff radius 2.5σ(Falk and Langer, 1998) to the center atom i. At the Nth plastic event, the local yield stress $\Delta\tau_c$ is computed centered at atom a_N with the maximum value of D_{min}^2 in the as-quenched configuration, and then this $\Delta\tau_{c,a_N}$ is compared with the distribution of $\Delta\tau_c$ above. To be consistent with the prior studies in the 2D LYS method (Barbot et al., 2018; Patinet et al., 2016), we quantify the correlation as

$$C_N = 1 - 2P_c\left(\Delta\tau_{c,a_N}\right), \tag{20}$$

where P_c is the cumulative distribution function of $\Delta\tau_c$.

For the first 200 identified plastic events, the correlation averaged over every 20 plastic events in 3 independent KA glasses is plotted against the number of the plastic event in Fig. 5(a). The corresponding total average with each R_{free} is presented in Fig. 5(b). The local yield stress ($\Delta\tau_c$) computed for $R_{free} = 5\sigma$ exhibits the highest total averaged correlation with the plastic events. The mean correlation with $R_{free} = 5\sigma$ remains positive through $\sim 2.5\%$ strain, about $1/3$ of the yielding strain. The correlation of the first plastic event is shown separately by the solid markers in Fig. 5(a), and these correlations decay rapidly with the number of plastic events with larger R_{free} values. The predictivity of the local yield stress method in 3D appears reasonably good in this preliminary study in which we consider only the local probing that perfectly aligns with the deformation imposed at the box boundary. This optimal $R_{free} \sim 5\sigma$ is consistent with the length scale of the prior study in the 2D LYS method (Barbot et al., 2018; Patinet et al., 2016), but the corresponding volume is significantly more substantial with $600 \sim 700$ atoms in each probing region in 3D.

We note that there exist some negative correlations in Fig. 5(a) and (b). As discussed in the previous 2D LYS studies (Barbot et al., 2018), the LYS measurements using larger values of R_{free} fail to account for the secondary STZs because their signature is obscured by other nearby low yield-stress STZs. In other words, spatial resolution is lost by increasing local patch size. This leads to rapid decay in the correlation at higher strains. The fact that off-axis rearrangements were not probed is also expected to result in the over-estimation of the local yield stress ($\Delta\tau_c$).

7. Variation in orientation, rotation and triaxiality

We expect that the local yield stress ($\Delta\tau_c$) is anisotropic in glasses. To explore this anisotropy, we vary the local probing and explore the $\Delta\tau_c$ yield surface in a democratic way at the optimal probing radius of $R_{free} = 5\sigma$. For this purpose, we transform E_u^L to a rotated unit strain E_u^{L*} by applying the rotation matrix $\boldsymbol{R}\left(\vec{O}(\alpha,\beta),\gamma\right)$

$$E_u^{L*} = \boldsymbol{R}^T\left(\vec{O}(\alpha,\beta),\gamma\right) E_u^L \boldsymbol{R}\left(\vec{O}(\alpha,\beta),\gamma\right). \tag{21}$$

In order to maintain an orthogonal simulation box, we rotate the atoms in the local region such that the principal axes of E_u^L align with the basis vectors that define the simulation box, illustrated in Fig. 6. $\boldsymbol{R}\left(\vec{O}(\alpha,\beta),\gamma\right)$ represents the general rotation tensor
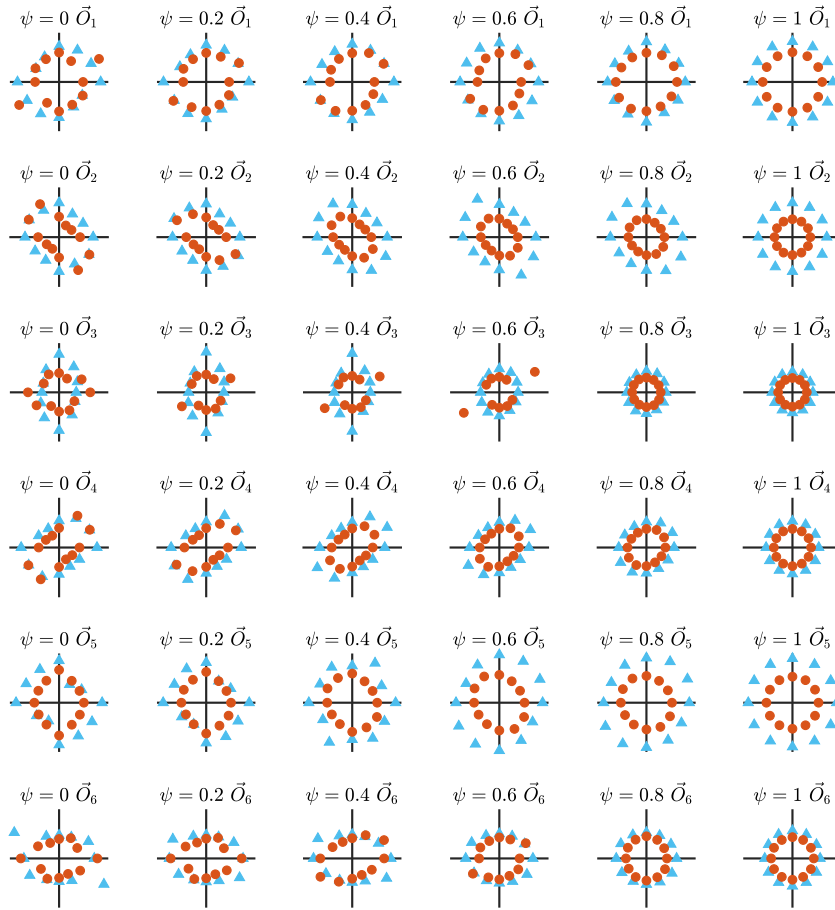
Fig. 7. $\Delta\tau_c$ with variation in triaxiality ψ horizontally and orientation $\vec{O}$ vertically. In each subplot, rotation angle γ is plotted as the angle counterclockwise from the horizontal axis pointing to the right, and the magnitude of $\Delta\tau_c$ is represented by the distance from the origin. Blue $\triangle$ and red $\circ$ denote the results for $\omega = -1$ and $+1$ in Eq. (22) respectively. All subplots are scaled with the limits of the axes as $5\epsilon/\sigma^3$.
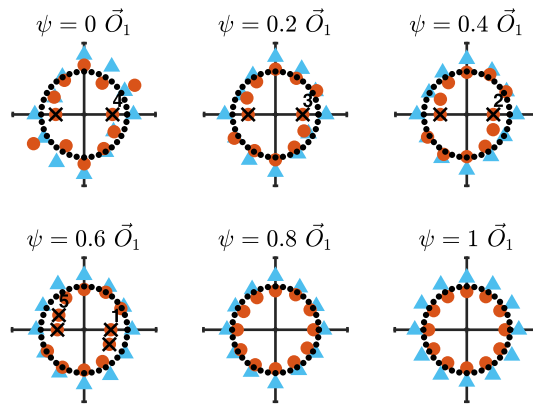*Source:* The original data can be found on Johns Hopkins University Data Archive (Ruan et al., 2021).

Fig. 8. Projected local yield stress ($\Delta\tau_y$) calculated by Eq. (25) to (27) with E_u^G in Eq. (11). Only $\Delta\tau_y$ with $\vec{O}_1$ is plotted corresponding to the 1st row in Fig. 7. Black crosses mark the five lowest values of $\Delta\tau_y$ with labeling 1 next to the smallest value. The black dotted circle labels the magnitude of the minimum $\Delta\tau_y$ among all other $\vec{O}$ orientations as a reference in each plot. All subplots are scaled with the limits of the axes as $5\epsilon/\sigma^3$.
Source: The original data can be found on Johns Hopkins University Data Archive (Ruan et al., 2021).

expressed as a function of $\vec{O}$, an arbitrary unit vector with which the x axis is brought into alignment, specified in terms of (α, β), a polar and an azimuthal angle respectively, and γ, an angle that describes a prior rotation about the x axis. To sample $\vec{O}$ evenly in 3D, we utilize the face norms of a regular dodecahedron. The resulting rotation is illustrated in Fig. 6. The atoms within the cut-out sphere are first rotated by an angle γ counterclockwise about $\vec{X}_a$ that is then rotated to align with a direction $\vec{O}$. After the rotation operation is applied on the atoms, a loading E_u^L is imposed on the local boundary. The deformation imposed on the principal axes may be expressed in terms of triaxiality ψ as

$$E_u^L = \frac{\omega\sqrt{2\psi^2 - 4\psi + 8}}{\psi^2 - 2\psi + 4} \begin{bmatrix} 1 & 0 & 0 \\ 0 & \frac{\psi}{2} - 1 & 0 \\ 0 & 0 & -\frac{\psi}{2} \end{bmatrix}, \tag{22}$$

where, $\omega = -1$ (x-axis compression) or $+1$ (x-axis tension). ψ ranges from 0 to 1 inclusively, and in doing so determines the symmetry of the loading. If $\psi = 0$,

$$E_u^L = \frac{\omega\sqrt{2}}{2} \begin{bmatrix} 1 & 0 & 0 \\ 0 & -1 & 0 \\ 0 & 0 & 0 \end{bmatrix}, \tag{23}$$

and a pure shear loading strain is thus applied. With zero strain along z axis, this plane strain deformation recovers the local probing studied in the prior work regarding the two-dimensional LYS method (Patinet et al., 2016; Barbot et al., 2018). As ψ increases to 1,

$$E_u^L = \frac{\omega\sqrt{6}}{2} \begin{bmatrix} 1 & 0 & 0 \\ 0 & -\frac{1}{2} & 0 \\ 0 & 0 & -\frac{1}{2} \end{bmatrix}, \tag{24}$$

resulting in a biaxial loading that is symmetric about the x axis.

For the sake of a preliminary study regarding the anisotropy of the local yield stress ($\Delta\tau_c$), we focus on the region centered around the single atom with the most dramatic plastic rearrangement as characterized by D_{min}^2 from Eq. (19) applied to the first plastic event identified in Fig. 3 during the deformation of a 3D KA glass. When computing $\Delta\tau_c$, we choose $R_{free} = 5\sigma$ as the optimal length scale in the LYS method. Then we systematically vary the triaxiality ψ to take the values 0, 0.2, 0.4, 0.6, 0.8, and 1.0. At each ψ, we consider 6 orientation directions of $\vec{O}(\alpha, \beta)$ as shown in the middle of Fig. 6. For each $\vec{O}(\alpha, \beta)$, the rotation angle γ is set to be 0°, 30°, 60°, 90°, 120°, and 150°.

In Fig. 7, the calculated local yield stresses ($\Delta\tau_c$) are presented in a series of 2D plots with variation in rotation (γ), orientation ($\vec{O}$), triaxiality (ψ) and loading direction (ω). Each plot corresponds to a chosen set of ψ and $\vec{O}$, and the resulting $\Delta\tau_c$ from both compressive and tensile loadings are plotted for each value of γ. As expected, the projection must be a circle when $\psi = 1$ since this corresponds to equibiaxial loading, and E_u^L in Eq. (24) is symmetric about the x axis in this case. As ψ decreases to 0 (from right to left), $\Delta\tau_c$ loses this symmetry. The resulting $\Delta\tau_c$ projections from both loading directions ($\omega = -1, +1$) are consistent in their elongation, and it is generally the case that the x-axis compressive $\Delta\tau_c$ is slightly larger in magnitude than its corresponding x-axis tensile $\Delta\tau_c$, particularly for larger values of ψ.

Although the as-quenched glass structure is statistically isotropic with respect to orientation and rotation, the data in Fig. 7 clearly shows that locally the plastic response can be highly anisotropic. Variations of more than a factor of two in yield stress are found as we scan the full range orientations, particularly as we vary orientation or move away from equibiaxial loading ($\psi=1$). This is particularly evident in the difference between orientations 1 (the first row) and 3 (the third row). The expected consequence of this is that the spatial orientation of the resulting plastic shear may reasonably be expected to vary from that of the applied load if the weakest orientation is misaligned to the applied shear loading.

In previous sections, the deformation on the box boundary given by E_u^G is identical to the shear of the local probing used to analyze the local value of $\Delta\tau_c$ given by E_u^L. Here, we are able to cross-compare the propensity for the applied global loading to trigger the local yield stresses ($\Delta\tau_c$) measured along multiple probing directions, projecting each $\Delta\tau_c$ along the applied loading direction by calculating

$$f_p^2 = E_u^{L*} : E_u^G, \tag{25}$$

$$p_f = \frac{f_p^2}{|f_p^2|}\sqrt{|f_p^2|}, \tag{26}$$

such that the projected local yield stress is expressed as

$$\Delta\tau_y = \frac{\Delta\tau_c}{p_f}. \tag{27}$$

If $E_u^{L*} = E_u^G$, then $p_f = 1$ and the deformation on the box boundary aligns perfectly with the local probing when computing $\Delta\tau_c$. This is the case for our results in the previous sections. If $0 < p_f < 1$, the stress along E_u^G must be greater than $\Delta\tau_c$ itself in order to trigger the same local rearrangement probed by E_u^{L*}. If $p_f < 0$, it indicates that the loading via E_u^G contributes in the opposite

direction as that applied during the local probing E_u^{L*}. This should indicate that it is impossible to trigger such a rearrangement by applying this E_u^G.

The projected local yield stresses ($\Delta\tau_y$) along E_u^G in Eq. (11) are mapped in Fig. 8 with the same presentation as in Fig. 7. Due to the fact that $\Delta\tau_y$ varies over a very large range, from $-20\epsilon/\sigma^3$ to $20\epsilon/\sigma^3$ after being scaled by p_f in Eq. (27), we only present the resultant $\Delta\tau_c$ with $\vec{O}_1$ corresponding to the 1st row in Fig. 7, which are found to be generally lower in magnitude than those in other orientation directions. With all negative $\Delta\tau_y$ values neglected, all subplots are scaled to a radius of $5\epsilon/\sigma^3$. The minimum positive $\Delta\tau_y$ along all other $\vec{O}$ orientations is indicated by black dotted circles as a reference in each plot. The black crosses label the five smallest positive $\Delta\tau_y$ values. The $\Delta\tau_y$ locally probed with E_u^L in Eq. (6) ranks as the 4th least in its value. This E_u^L aligns perfectly with E_u^G in the prior section, and the difference from the lowest $\Delta\tau_y$ is $\sim 8\%$ and is small in comparison to the highest level of the $\Delta\tau_y$ scale, $20\epsilon/\sigma^3$. This indicates that, as expected, the easiest-to-trigger local rearrangement does not necessarily align with the loading imposed at the boundary, and the difference between the two appears to predominantly associated with the triaxiality ψ.

We are also curious to compare the triaxiality ψ of the corresponding local rearrangement centered at this targeted atom when applying E_u^G on the boundary. The atomic strain with averaging radius 5σ is computed according to Eq. (15) by comparing the yielding configuration with the initial state. This strain tensor is an 'average' over the probing region, and this can be compared to the local probing presented by the effective unit strain tensor E_u^{L*} in Eq. (21) after normalization. Accordingly, the eigenvalues of the normalized atomic strain tensor are then compared to E_u^L in Eq. (22) and the resulting value of ψ is 0.465. This value falls between $\psi = 0.4$ and $\psi = 0.6$ which correspond to the 2nd and the 1st lowest $\Delta\tau_y$ marked in Fig. 8. In addition, the p_f between the probing E_u^{L*} and the above averaged atomic strain yields ~ 0.938 for the minimal $\Delta\tau_y$ higher than $p_f \sim 0.896$ found for the $\Delta\tau_y$ when the local regions are probed aligning perfectly with the loading on the boundary (the 4th lowest). This high degree of correspondence indicates that the triggered local plastic event is not necessarily in alignment with the loading on the boundary, but, rather the local arrangement could be well predicted by the minimum $\Delta\tau_y$ from the local yield surface. The correlation might be improved if a more complete range of local probing were undertaken at each sampling point, particularly with respect to the triaxiality ψ.

We also note that in producing this data set we have not systematically varied the hydrostatic loading; only the orientation and triaxiality of shear was varied. Prior studies in two-dimensions have indicated a modest linear dependence of yield stress on pressure, consistent with experimental results (Lund and Schuh, 2003; Barbot et al., 2020). We expect that is also the case for this system, but confirming this is left for future work.

8. Conclusions

By applying the local yield stress (LYS) method to a computational model of a three-dimensional glass and varying the local probing over a range of triaxialities (ψ), orientations ($\vec{O}(\alpha, \beta)$), rotations (γ), and directions (ω), we are able to obtain a sense of the complexity of the response of the glass microstructure when subjected to shear. We note that the optimal length scale for this analysis (approximately 5 atomic diameters in radius) is just above the smallest length scale at which the 3D Hooke's law remains valid, as was the case in 2D, although significantly more atoms reside within the resulting probing region (600–700 atoms) due to the higher dimensionality. When we are limited to probing at a shear identical to the loading on the boundary, the mean correlation after noise reduction persists through the first 200 identified plastic events or 1/3 the yielding strain ($\sim 7\%$). The local yield stress surface is significantly anisotropic. And the projected local yield stresses ($\Delta\tau_y$) with respect to the loading on the boundary does a very good job of predicting the sense of the shear at the first yield event. It is thus anticipated that the correlation of the yield stress analysis might be improved by characterizing the entire yield surface, rather than only the shear commensurate with that applied at the boundary, on each sampling point.

This detailed glimpse into the local yield surfaces present in a three-dimensional model glass has clear relevance for guiding the development of constitutive models. Many coarse-grained mesoscale theories have been developed based on the concepts of local yield (Nicolas et al., 2018). However, the underlying statistics of the local yield distribution have been a matter of significant debate. Here we show that depending on the scale of the coarse-graining, an assumption of Weibull statistics is applicable. We also show that the power-law tail of the Weibull distribution converges to a value $(b - 1) \lesssim 0.71$ that is consistent with numerical estimates (Karmakar et al., 2010) and predictions of nonlinear quasilocalized excitation scaling. (Kapteijns et al., 2020) However, this Weibull fit appears not to arise from simple "weakest link" statistics. At this time we can only conjecture that the discrepancy between the underlying distribution and the larger scale Weibull fit arises from elastic effects that emerge on longer length scales, modulus fluctuations, or STZ interactions.

We also see evidence of the relevance of both the distribution of yield stresses along a particular sense of loading and the shape of the local yield surface. This has clear consequences for where yield will be triggered and anticipates that such theories should account for potential misalignment between the applied load and the resulting plastic flow. Our work also highlights one particular outstanding question: How can we best characterize these local yield surfaces? They are not simply random, but rather exhibit relatively smooth and regularly varying shapes. It is our belief that only by constructing a reliable reduced description of these complex stochastic yield surfaces can one effectively experimentally characterize the mechanical response of these fascinating structurally disordered materials.

Declaration of competing interest

The authors declare that they have no known competing financial interests or personal relationships that could have appeared to influence the work reported in this paper.

Acknowledgments

Appendix A. Sample preparation

In each sample, 1,000,000 atoms are simulated in a cubic simulation box with periodic boundary conditions along the x, y and z axes. The system is comprised of 80% large atoms (A) and 20% small atoms (B). We apply a smoothed 6–12 Lennard-Jones(LJ) potential to quantify the interatomic interactions as follows Barbot et al. (2018):

When $r \leq r_{in}$,

$$U_{\alpha\beta}(r) = 4\epsilon_{\alpha\beta} \left[\left(\frac{\sigma_{\alpha\beta}}{r} \right)^{12} - \left(\frac{\sigma_{\alpha\beta}}{r} \right)^{6} \right] + C', \tag{A.1}$$

When $r_{in} < r \leq r_{out}$,

$$U_{\alpha\beta}(r) = C_0 + C_1(r - r_{in}) + C_2(r - r_{in})^2 + C_3(r - r_{in})^3 + C_4(r - r_{in})^4, \tag{A.2}$$

When $r > r_{out}$,

$$U_{\alpha\beta}(r) = 0, \tag{A.3}$$

with

$$C' = C_0 - 4\epsilon_{\alpha\beta} \left[\left(\frac{\sigma_{\alpha\beta}}{r_{in}} \right)^{12} - \left(\frac{\sigma_{\alpha\beta}}{r_{in}} \right)^{6} \right], \tag{A.4}$$

$$C_0 = -(r_{out} - r_{in}) \left[3C_1 + C_2(r_{out} - r_{in}) \right] / 6, \tag{A.5}$$

$$C_1 = 24\epsilon_{\alpha\beta}\sigma_{\alpha\beta}^6(r_{in}^6 - 2\sigma_{\alpha\beta}^6)/r_{in}^{13}, \tag{A.6}$$

$$C_2 = 12\epsilon_{\alpha\beta}\sigma_{\alpha\beta}^6(26\sigma_{\alpha\beta}^6 - 7r_{in}^6)/r_{in}^{14}, \tag{A.7}$$

$$C_3 = -[3C_1 + 4C_2(r_{out} - r_{in})]/[3(r_{out} - r_{in})^2], \tag{A.8}$$

$$C_4 = [C_1 + C_2(r_{out} - r_{in})]/[2(r_{out} - r_{in})^3]. \tag{A.9}$$

α and β denote particle species A or B. In LJ units, all quantities are represented in terms of particle mass m, which is equivalent for both species, interatomic distance σ, and interaction energy ϵ. Consequently, time is measured in units of $t_0 = \sigma\sqrt{m/\epsilon}$, temperature in units of ϵ/k_B, pressure and stress in units of ϵ/σ^3, etc. In the Kob and Andersen (1995) model, the bonding energies are $\epsilon_{AA} = 1.0\epsilon$, $\epsilon_{BB} = 0.5\epsilon$, $\epsilon_{AB} = \epsilon_{BA} = 1.5\epsilon$, and the equilibrium particle spacings are $\sigma_{AA} = 1.0\sigma$, $\sigma_{AA} = 0.88\sigma$, $\sigma_{AB} = \sigma_{BA} = 0.8\sigma$.(Shi and Falk, 2006) This potential field is smoothed from $r_{in} = 2.0\sigma$ to $r_{out} = 2.5\sigma$ via a polynomial function with coefficients C_0, C_1, C_2, C_3 and C_4 as shown in Eq. (A.2), to avoid any discontinuity in the force associated with the potential's short-ranged cutoff.

Appendix B. Deviation from Hooke's law

B.1. Elastic constants for the bulk glasses

To estimate the bulk elastic constants, the simulation box is loaded independently along xx, yy, zz, or sheared along xy, xz, yz up to 1×10^{-7} strain using the athermal quasi-static (AQS) method (Tanguy et al., 2006; Lerner and Procaccia, 2009; Tsamados et al., 2009; Dasgupta et al., 2012; Karmakar et al., 2010; Maloney and Lemaître, 2004). After strain is applied along each of the six probing directions, the elastic constants are calculated such that

$$c_{AB} = s_A/e_B \tag{B.1}$$

with A and B taking the values xx, yy, zz, xy, xz, or yz. For each loading, both positive and negative strain are applied and averaged. The $c_{AB} = c_{BA}$ elements are symmetrized as $(c_{AB} + c_{BA})/2$ for the off-diagonal elastic constants.
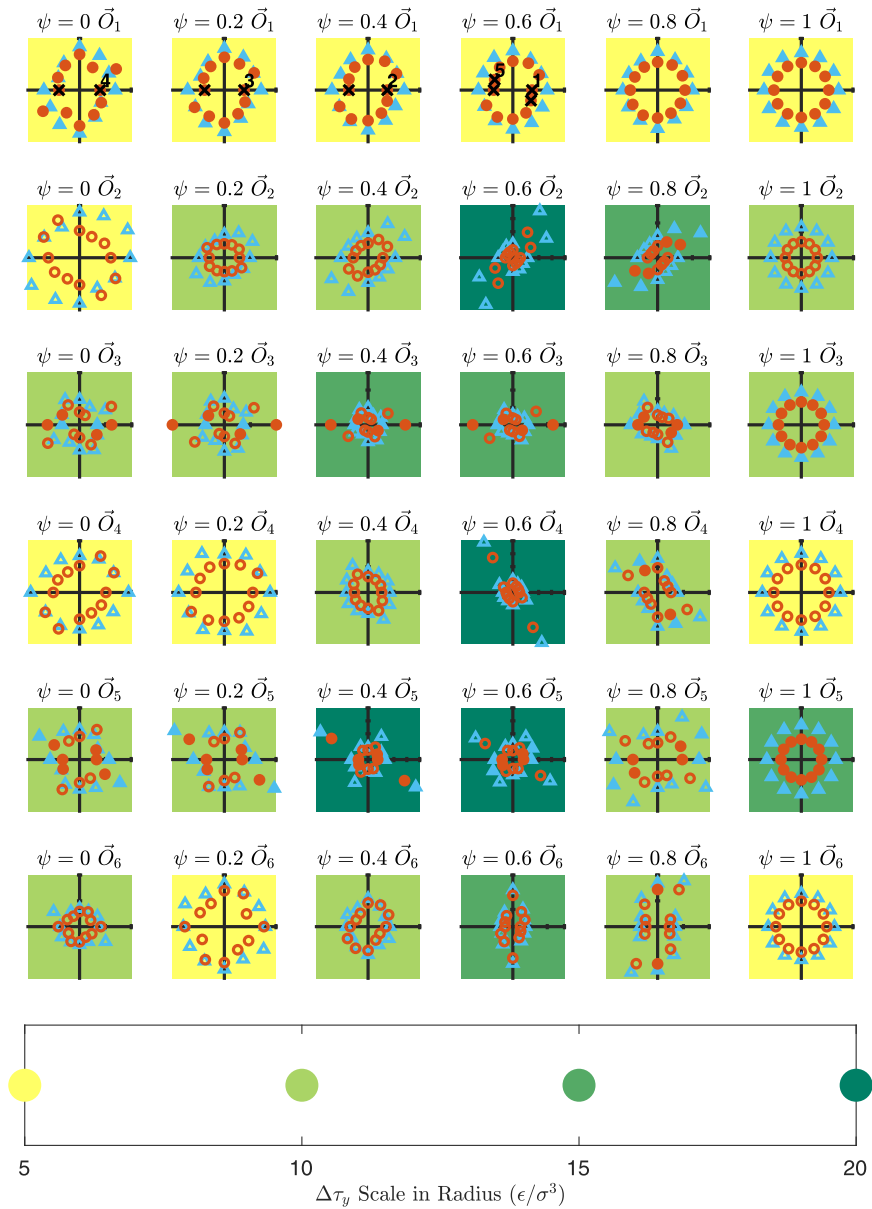
Fig. C.9. Projected local yield stress ($\Delta\tau_y$).

Appendix C. Variation in orientation, rotation and triaxiality

The projected local yield stress $\Delta\tau_y$

The patterns of the Projected Local Yield Stress $\Delta\tau_y$ are presented in Fig. C.9. In the array of plots, triaxiality (ψ) is varied horizontally and orientation ($\vec{O}$) is varied vertically. In each plot, rotation angle (γ) is the angle counterclockwise from the horizontal axis pointing to the right, and the magnitude of $\Delta\tau_c$ is represented by the distance from the origin. Blue △ and red ∘ denote the results for $\omega = -1$ and $+1$. Black crosses mark the five lowest values of $\Delta\tau_y$ where the label 1 indicates the smallest value. In addition, solid and hollow markers denote positive and negative sign respectively. In order to show the full range of values, each plot is scaled with the limits of the axes varied to ±5, ±10, ±15, and $\pm20\epsilon/\sigma^3$, and this variation in scaling is denoted by the yellow, light green, green, and dark green backgrounds, as is shown in the bottom subplot.

References

Barbot, A., Lerbinger, M., Hernandez-Garcia, A., García-García, R., Falk, M.L., Vandembroucq, D., Patinet, S., 2018. Local yield stress statistics in model amorphous solids. Phys. Rev. E 97 (3), 033001. http://dx.doi.org/10.1103/PhysRevE.97.033001.

Barbot, A., Lerbinger, M., Lemaitre, A., Vandembroucq, D., Patinet, S., 2020. Rejuvenation and shear banding in model amorphous solids. Phys. Rev. E 101 (3), 033001. http://dx.doi.org/10.1103/PhysRevE.101.033001.

Bouchbinder, E., Langer, J., 2009a. Nonequilibrium thermodynamics of driven amorphous materials. I. Internal degrees of freedom and volume deformation. Phys. Rev. E 80 (3), 031131. http://dx.doi.org/10.1103/PhysRevE.80.031131.

Bouchbinder, E., Langer, J., 2009b. Nonequilibrium thermodynamics of driven amorphous materials. II. Effective-temperature theory. Phys. Rev. E 80 (3), 031132. http://dx.doi.org/10.1103/PhysRevE.80.031132.

Bouchbinder, E., Langer, J., 2009c. Nonequilibrium thermodynamics of driven amorphous materials. III. Shear-transformation-zone plasticity. Phys. Rev. E 80 (3), 031133. http://dx.doi.org/10.1103/PhysRevE.80.031133.

Bouchbinder, E., Langer, J., Procaccia, I., 2007a. Athermal shear-transformation-zone theory of amorphous plastic deformation. I. Basic principles. Phys. Rev. E 75 (3), 036107. http://dx.doi.org/10.1103/PhysRevE.75.036107.

Bouchbinder, E., Langer, J., Procaccia, I., 2007b. Athermal shear-transformation-zone theory of amorphous plastic deformation. II. Analysis of simulated amorphous silicon. Phys. Rev. E 75 (3), 036108. http://dx.doi.org/10.1103/PhysRevE.75.036108.

Chen, Y., Diaz, A., 2018. Physical foundation and consistent formulation of atomic-level fluxes in transport processes. Phys. Rev. E 98 (5), 052113. http://dx.doi.org/10.1103/PhysRevE.98.052113.

Cubuk, E., Schoenholz, S., Rieser, J., Malone, B., Rottler, J., Durian, D., Kaxiras, E., Liu, A., 2015. Identifying structural flow defects in disordered solids using machine-learning methods. Phys. Rev. Lett. 114 (10), 108001. http://dx.doi.org/10.1103/PhysRevLett.114.108001.

Dasgupta, R., Karmakar, S., Procaccia, I., 2012. Universality of the plastic instability in strained amorphous solids. Phys. Rev. Lett. 108 (7), 075701. http://dx.doi.org/10.1103/PhysRevLett.108.075701.

Ding, J., Cheng, Y.-Q., Ma, E., 2014a. Full icosahedra dominate local order in Cu64Zr34 metallic glass and supercooled liquid. Acta Mater. 69, 343–354. http://dx.doi.org/10.1016/j.actamat.2014.02.005.

Ding, J., Patinet, S., Falk, M.L., Cheng, Y., Ma, E., 2014b. Soft spots and their structural signature in a metallic glass. Proc. Natl. Acad. Sci. 111 (39), 14052–14056. http://dx.doi.org/10.1073/pnas.1412095111.

Falk, M., Langer, J., 1998. Dynamics of viscoplastic deformation in amorphous solids. Phys. Rev. E 57 (6), 7192–7205. http://dx.doi.org/10.1103/PhysRevE.57.7192.

Gartner, L., Lerner, E., 2016. Nonlinear plastic modes in disordered solids. Phys. Rev. E 93 (1), 011001. http://dx.doi.org/10.1103/PhysRevE.93.011001.

Gumbel, E.J., 2004. Statistics of Extremes. Dover Publications, Mineola, N.Y..

Hansen, A., Roux, S., 2000. Statistics toolbox for damage and fracture. In: Krajcinovic, D., Van Mier, J. (Eds.), Damage and Fracture of Disordered Materials. In: International Centre for Mechanical Sciences, Springer, Vienna, pp. 17–101. http://dx.doi.org/10.1007/978-3-7091-2504-5_2.

Heyes, D., 1994. Pressure tensor of partial-charge and point-dipole lattices with bulk and surface geometries. Phys. Rev. B 49 (2), 755–764. http://dx.doi.org/10.1103/PhysRevB.49.755.

Hinkle, A.R., Rycroft, C.H., Shields, M.D., Falk, M.L., 2017. Coarse graining atomistic simulations of plastically deforming amorphous solids. Phys. Rev. E 95 (5), 053001. http://dx.doi.org/10.1103/PhysRevE.95.053001.

Homer, E.R., Schuh, C.A., 2009. Mesoscale modeling of amorphous metals by shear transformation zone dynamics. Acta Mater. 57 (9), 2823–2833. http://dx.doi.org/10.1016/j.actamat.2009.02.035.

Hoover, W.G., 1985. Canonical dynamics: Equilibrium phase-space distributions. Phys. Rev. A 31 (3), 1695–1697. http://dx.doi.org/10.1103/PhysRevA.31.1695.

Jiang, F., Jiang, M., Wang, H., Zhao, Y., He, L., Sun, J., 2011. Shear transformation zone volume determining ductile–brittle transition of bulk metallic glasses. Acta Mater. 59 (5), 2057–2068. http://dx.doi.org/10.1016/j.actamat.2010.12.006.

Jiang, R., Murthy, D., 2011. A study of Weibull shape parameter: properties and significance. Reliab. Eng. Syst. Saf. 96 (12), 1619–1626. http://dx.doi.org/10.1016/j.ress.2011.09.003.

Jones, J., Chapman, S., 1924. On the determination of molecular fields. —II. From the equation of state of a gas. Proc. R. Soc. Lond. Ser. A Math. Phys. Eng. Sci. 106 (738), 463–477. http://dx.doi.org/10.1098/rspa.1924.0082.

Kapteijns, G., Richard, D., Lerner, E., 2020. Nonlinear quasilocalized excitations in glasses: true representatives of soft spots. Physical Review E 101 (3), 032130. http://dx.doi.org/10.1103/PhysRevE.101.032130.

Karmakar, S., Lerner, E., Procaccia, I., 2010. Statistical physics of the yielding transition in amorphous solids. Phys. Rev. E 82 (055103(R)), http://dx.doi.org/10.1103/PhysRevE.82.055103.

Kob, W., Andersen, H.C., 1995. Testing mode-coupling theory for a supercooled binary Lennard-Jones mixture I: The van Hove correlation function. Phys. Rev. E 51 (5), 4626–4641. http://dx.doi.org/10.1103/PhysRevE.51.4626.

Kontolati, K., Alix-Williams, D., Boffi, N.M., Falk, M.L., Rycroft, C.H., Shields, M.D., 2021. Manifold learning for coarse-graining atomistic simulations: Application to amorphous solids. arXiv:2103.00779 [Physics].

LAMMPS, Large-Scale Atomic/Molecular Massively Parallel Simulator, http://lammps.sandia.gov.

Lerner, E., Procaccia, I., 2009. Locality and nonlocality in elastoplastic responses of amorphous solids. Phys. Rev. E 79 (6), 066109. http://dx.doi.org/10.1103/PhysRevE.79.066109.

LeSar, R., 2014. Simulations of dislocation structure and response. Annu. Rev. Condensed Matter Phys. 5 (1), 375–407. http://dx.doi.org/10.1146/annurev-conmatphys-031113-133858.

Lund, A.C., Schuh, C.A., 2003. Yield surface of a simulated metallic glass. Acta Mater. 51 (18), 5399–5411.

Ma, Y., Ye, J., Peng, G., Wen, D., Zhang, T., 2015a. Loading rate effect on the creep behavior of metallic glassy films and its correlation with the shear transformation zone. Mater. Sci. Eng. A 622, 76–81. http://dx.doi.org/10.1016/j.msea.2014.11.022.

Ma, Y., Ye, J., Peng, G., Wen, D., Zhang, T., 2015b. Nanoindentation study of size effect on shear transformation zone size in a Ni–Nb metallic glass. Mater. Sci. Eng. A 627, 153–160. http://dx.doi.org/10.1016/j.msea.2015.01.001.

Maloney, C., Lemaître, A., 2004. Universal breakdown of elasticity at the onset of material failure. Phys. Rev. Lett. 93 (19), 195501. http://dx.doi.org/10.1103/PhysRevLett.93.195501.

Manning, M., Langer, J., Carlson, J., 2007. Strain localization in a shear transformation zone model for amorphous solids. Phys. Rev. E 76 (5), 056106. http://dx.doi.org/10.1103/PhysRevE.76.056106.

Manning, M., Liu, A., 2011. Vibrational modes identify soft spots in a sheared disordered packing. Phys. Rev. Lett. 107 (10), 108302. http://dx.doi.org/10.1103/PhysRevLett.107.108302.

Mizuno, H., Mossa, S., Barrat, J.-L., 2013. Measuring spatial distribution of local elastic modulus in glasses. Phys. Rev. E 87, 042306. http://dx.doi.org/10.1103/PhysRevE.87.042306.

Nicolas, A., Ferrero, E.E., Martens, K., Barrat, J.-L., 2018. Deformation and flow of amorphous solids: Insights from elastoplastic models. Rev. Modern Phys. 90 (4), 045006.

Nosé, S., 1984. A unified formulation of the constant temperature molecular dynamics methods. J. Chem. Phys. 81 (1), 511–519. http://dx.doi.org/10.1063/1.447334.

Paige, C.C., Saunders, M.A., 1982. LSQR: an algorithm for sparse linear equations and sparse least squares. ACM Trans. Math. Software 8 (1), 43–71. http://dx.doi.org/10.1145/355984.355989.

Pan, D., Yokoyama, Y., Fujita, T., Liu, Y., Kohara, S., Inoue, A., Chen, M., 2009. Correlation between structural relaxation and shear transformation zone volume of a bulk metallic glass. Appl. Phys. Lett. 95 (14), 141909. http://dx.doi.org/10.1063/1.3246151.

Parrinello, M., Rahman, A., 1981. Polymorphic transitions in single crystals: A new molecular dynamics method. J. Appl. Phys. 52 (12), 7182–7190. http://dx.doi.org/10.1063/1.328693.

Patinet, S., Vandembroucq, D., Falk, M.L., 2016. Connecting local yield stresses with plastic activity in amorphous solids. Phys. Rev. Lett. 117 (4), 045501. http://dx.doi.org/10.1103/PhysRevLett.117.045501.

Polak, E., Ribiere, G., 1969. Note sur la convergence de méthodes de directions conjuguées. Rev. Fr. Inf. Rech. Erationnelle. Sér. Rouge 3 (16), 35–43. http://dx.doi.org/10.1051/m2an/196903R100351.

Priezjev, N.V., 2017. Collective nonaffine displacements in amorphous materials during large-amplitude oscillatory shear. Phys. Rev. E 95 (2), 023002. http://dx.doi.org/10.1103/PhysRevE.95.023002.

Püschl, W., 2002. Models for dislocation cross-slip in close-packed crystal structures: A critical review. Prog. Mater. Sci. 47 (4), 415–461. http://dx.doi.org/10.1016/S0079-6425(01)00003-2.

Richard, D., Kapteijns, G., Giannini, J.A., Manning, M.L., Lerner, E., 2021. Simple and broadly applicable definition of shear transformation zones. Phys. Rev. Lett. 126 (1), 015501. http://dx.doi.org/10.1103/PhysRevLett.126.015501.

Richard, D., Ozawa, M., Patinet, S., Stanifer, E., Shang, B., Ridout, S., Xu, B., Zhang, G., Morse, P., Barrat, J.-L., Berthier, L., Falk, M., Guan, P., Liu, A., Martens, K., Sastry, S., Vandembroucq, D., Lerner, E., Manning, M., 2020. Predicting plasticity in disordered solids from structural indicators. Phys. Rev. Mater. 4 (11), 113609. http://dx.doi.org/10.1103/PhysRevMaterials.4.113609.

Ruan, D., Patinet, S., Falk, M.L., 2021. Data Associated with the Publication: Predicting Plastic Events and Quantifying the Local Yield Surface in 3D Model Glasses. Johns Hopkins University Data Archive, http://dx.doi.org/10.7281/T1/HVRF8B.

Rycroft, C.H., Sui, Y., Bouchbinder, E., 2015. An Eulerian projection method for quasi-static elastoplasticity. J. Comput. Phys. 300, 136–166. http://dx.doi.org/10.1016/j.jcp.2015.06.046, arXiv:1409.2173.

Salerno, K.M., Robbins, M.O., 2013. Effect of inertia on sheared disordered solids: Critical scaling of avalanches in two and three dimensions. Phys. Rev. E 88 (6), 062206. http://dx.doi.org/10.1103/PhysRevE.88.062206.

Schoenholz, S., Cubuk, E., Sussman, D., Kaxiras, E., Liu, A., 2016. A structural approach to relaxation in glassy liquids. Nat. Phys. 12 (5), 469–471. http://dx.doi.org/10.1038/nphys3644.

Schuh, C.A., Lund, A.C., 2003. Atomistic basis for the plastic yield criterion of metallic glass. Nature Mater. 2 (7), 449–452. http://dx.doi.org/10.1038/nmat918.

Shang, B., Rottler, J., Guan, P., Barrat, J.-L., 2019. Local versus global stretched mechanical response in a supercooled liquid near the glass transition. Phys. Rev. Lett. 122 (10), 105501. http://dx.doi.org/10.1103/PhysRevLett.122.105501.

Shi, Y., Falk, M.L., 2005. Strain localization and percolation of stable structure in amorphous solids. Phys. Rev. Lett. 95 (9), 095502. http://dx.doi.org/10.1103/PhysRevLett.95.095502.

Shi, Y., Falk, M.L., 2006. Atomic-scale simulations of strain localization in three-dimensional model amorphous solids. Phys. Rev. B 73 (21), 214201. http://dx.doi.org/10.1103/PhysRevB.73.214201.

Shi, Y., Falk, M.L., 2007. Stress-induced structural transformation and shear banding during simulated nanoindentation of a metallic glass. Acta Mater. 55 (13), 4317–4324. http://dx.doi.org/10.1016/j.actamat.2007.03.029.

Shi, Y., Katz, M.B., Li, H., Falk, M.L., 2007. Evaluation of the disorder temperature and free-volume formalisms via simulations of shear banding in amorphous solids. Phys. Rev. Lett. 98 (18), 185505. http://dx.doi.org/10.1103/PhysRevLett.98.185505.

Shimizu, F., Ogata, S., Li, J., 2007. Theory of shear banding in metallic glasses and molecular dynamics calculations. Mater. Trans. 48 (11), 2923–2927. http://dx.doi.org/10.2320/matertrans.MJ200769.

Shockley, W., Read, W., 1949. Quantitative predictions from dislocation models of crystal grain boundaries. Phys. Rev. 75 (4), 692. http://dx.doi.org/10.1103/PhysRev.75.692.

Sirk, T.W., Moore, S., Brown, E.F., 2013. Characteristics of thermal conductivity in classical water models. J. Chem. Phys. 138 (6), 064505. http://dx.doi.org/10.1063/1.4789961.

Spaepen, F., 1977. A microscopic mechanism for steady state inhomogeneous flow in metallic glasses. Acta Metall. 25 (4), 407–415. http://dx.doi.org/10.1016/0001-6160(77)90232-2.

Stukowski, A., 2010. Visualization and analysis of atomistic simulation data with OVITO–the open visualization tool. Modelling Simulation Mater. Sci. Eng. 18 (1), 015012. http://dx.doi.org/10.1088/0965-0393/18/1/015012.

Stukowski, A., Albe, K., 2010. Extracting dislocations and non-dislocation crystal defects from atomistic simulation data. Modelling Simulation Mater. Sci. Eng. 18 (8), 085001. http://dx.doi.org/10.1088/0965-0393/18/8/085001.

Surblys, D., Matsubara, H., Kikugawa, G., Ohara, T., 2019. Application of atomic stress to compute heat flux via molecular dynamics for systems with many-body interactions. Phys. Rev. E 99 (5), 051301. http://dx.doi.org/10.1103/PhysRevE.99.051301.

Talamali, M., Petäjä, V., Vandembroucq, D., Roux, S., 2012. Strain localization and anisotropic correlations in a mesoscopic model of amorphous plasticity. Recent Advances in Micromechanics of Materials, C. R. Méc. Recent Advances in Micromechanics of Materials, 340 (4), 275–288.http://dx.doi.org/10.1016/j.crme.2012.02.010,

Tanguy, A., Leonforte, F., Barrat, J.-L., 2006. Plastic response of a 2D Lennard-Jones amorphous solid: Detailed analysis of the local rearrangements at very slow strain rate. Eur. Phys. J. E 20 (3), 355–364. http://dx.doi.org/10.1140/epje/i2006-10024-2.

Tanguy, A., Mantisi, B., Tsamados, M., 2010. Vibrational modes as a predictor for plasticity in a model glass. Europhys. Lett. 90 (1), 16004. http://dx.doi.org/10.1209/0295-5075/90/16004.

Thompson, A.P., Plimpton, S.J., Mattson, W., 2009. General formulation of pressure and stress tensor for arbitrary many-body interaction potentials under periodic boundary conditions. J. Chem. Phys. 131 (15), 154107. http://dx.doi.org/10.1063/1.3245303.

Tsamados, M., Tanguy, A., Goldenberg, C., Barrat, J.-L., 2009. Local elasticity map and plasticity in a model Lennard-Jones glass. Phys. Rev. E 80 (2), 026112. http://dx.doi.org/10.1103/PhysRevE.80.026112.

Weibull, W., Stockholm, S., 1951. A statistical distribution function of wide applicability. J. Appl. Mech. 18, 293–297. http://dx.doi.org/10.1115/1.4010337.

Widmer-Cooper, A., Perry, H., Harrowell, P., Reichman, D.R., 2008. Irreversible reorganization in a supercooled liquid originates from localized soft modes. Nat. Phys. 4 (9), 711–715. http://dx.doi.org/10.1038/nphys1025.

Xu, B., Falk, M., Li, J., Kong, L., 2017. Strain-dependent activation energy of shear transformation in metallic glasses. Phys. Rev. B 95 (14), 144201. http://dx.doi.org/10.1103/PhysRevB.95.144201.

Xu, B., Falk, M.L., Li, J., Kong, L., 2018. Predicting shear transformation events in metallic glasses. Phys. Rev. Lett. 120 (12), 125503. http://dx.doi.org/10.1103/PhysRevLett.120.125503.

Xu, B., Falk, M.L., Patinet, S., Guan, P., 2021. Atomic nonaffinity as a predictor of plasticity in amorphous solids. Phys. Rev. Mater. 5 (2), 025603. http://dx.doi.org/10.1103/PhysRevMaterials.5.025603.